energies

MDPI

Article

Advanced Control to Improve the Ramp-Rate of a Gas Turbine: Optimization of Control Schedule

Young-Kwang Park [1], Seong-Won Moon [1] and Tong-Seop Kim [2,*]

[1] Graduate School, Inha University, 100 Inha-ro, Michuhol-Gu, Incheon 22212, Korea; 22201210@inha.edu (Y.-K.P.); 22161642@inha.edu (S.-W.M.)
[2] Department of Mechanical Engineering, Inha University, 100 Inha-ro, Michuhol-Gu, Incheon 22212, Korea
* Correspondence: kts@inha.ac.kr; Tel.: +82-32-876-7308

Abstract: As the proportion of power generation using renewable energy increases, it is important to improve the operational flexibility of gas turbines (GTs) for the stability of power grids. Increasing the ramp-rate of GTs is a general solution. However, a higher ramp-rate increases the turbine inlet temperature (TIT), its rate of change, and the fluctuation of the frequency of produced electricity, which are negative side effects. This study proposes a method to optimize the set-point schedule for a PID controller to improve the ramp-rate while decreasing the negative impacts. The set-point schedule was optimized for a 170-MW class GT using a genetic algorithm to minimize the difference between the value of the process variable and the set-point value of the conventional control. The advanced control reduced the fluctuation of the rotation speed by 20% at the reference ramp-rates (12 MW/min and 15 MW/min). The maximum TIT decreased by 6.3 °C, and its maximum rate of change decreased from 0.7 °C/s to 0.4 °C/s. The advantage of the advanced control becomes more marked as the ramp-rate increases. Even at a much higher ramp-rate (50 MW/min), the advanced control decreased the rotation speed fluctuation by 40% in comparison to the conventional control at the reference ramp-rate.

Keywords: gas turbine; ramp-rate; dynamic simulation; set-point schedule; genetic algorithm

Citation: Park, Y.-K.; Moon, S.-W.; Kim, T.-S. Advanced Control to Improve the Ramp-Rate of a Gas Turbine: Optimization of Control Schedule. *Energies* **2021**, *14*, 8024. https://doi.org/10.3390/en14238024

Academic Editor: Andrzej Teodorczyk

Received: 25 October 2021
Accepted: 24 November 2021
Published: 1 December 2021

1. Introduction

1.1. Background and Motivation

As the global climate crisis becomes more serious, the issue of carbon neutrality is attracting attention worldwide. The International Energy Agency (IEA) [1] has presented several possible scenarios for carbon neutrality, and in all scenarios, the proportion of power generation using renewable energy increases rapidly. According to the sustainable development scenario (SDS), it is predicted that the proportion of power generation using renewable energy will be about 52% by 2030. As a result, carbon emissions in the electric power sector would decrease by more than 40% by 2030.

However, there is a disadvantage of power generation using renewable energy sources such as wind and solar energy: the power production is intermittent and depends on the weather conditions. Studies have analyzed problems such as the instability of power grids and frequency fluctuation caused by the intermittency of renewable energy [2,3]. A backup power system can solve this problem by compensating for the insufficient power supply. Studies have suggested gas turbines (GTs) and nuclear power [4,5] as backup power-generation systems as well as energy storage systems (ESSs) and fuel cells [6,7].

This study focused on GTs as a backup power-generation system. One of the major advantages of GTs is that they provide large inertia to the electric grid, which cannot be provided by most other new power-generation systems that generate direct current electricity such as wind power, photovoltaics, fuel cells, and EESs. The degree of frequency fluctuation of the power system depends on the system inertia [8], and the frequency fluctuations of GTs are relatively small due to their large rotating inertia [9,10]. Furthermore,

compared to other conventional power-generation systems such as coal-fired power plants and nuclear power plants, GTs have advantages of faster start-up and shut-down, flexible load-following operation, high specific power output, and low emission of pollutants.

Recently, various studies have been conducted to maximize the advantages of GTs. Studies have examined power-to-gas (P2G) systems that store surplus power output from renewable energy in the form of gaseous fuels such as hydrogen or methane [11]. Furthermore, studies have been conducted on power-to-liquid (P2L) systems that store liquid fuel [12]. Studies have also been conducted on the performance of a hybrid system that was combined with a carbon capture system, fuel cell, and GT [13]. Studies were also conducted on a hydrogen turbine using hydrogen as fuel [14].

With the increasing penetration of variable renewable energy, studies to improve the operational flexibility of GTs have become more important. For example, a report from the California Independent System Operator [15] predicted that the electricity demand from a backup power-generation system would rapidly increase as the proportion of solar power generation increases: a surge in the electricity demand of 10,000 MW in three hours was expected. A 2016 report from an energy consulting firm indicated that the actual electricity demand of California surged by 1146 MW more than expected and that the "duck curve" phenomenon has become more severe [16]. The duck curve is widely used to describe the severe imbalance between electricity demand and power generation. Therefore, a more flexible load-following operation of a GT is required to respond to the rapidly changing power demand. Furthermore, the operating environment of GTs has changed from base-load operation to partial-load operation in a wide range. Thus, analysis of the stability of a GT in a wide operation range is required.

1.2. Increase of GT Ramp-Rate for Operational Flexibility

Manufacturers have tried to improve operating flexibility by increasing the ramp-rate [17,18]. However, there is a limit to the improvement in the ramp-rate due to the control characteristics of GTs. At present, the GT power output is adjusted through schedule-based control [19,20]. In this method, the turbine exhaust temperature (TET) is scheduled in advance according to the compressor discharge pressure. When the GT power output changes, the fuel flow rate and the angle of the variable inlet guide vane (VIGV) are manipulated to satisfy the set-point of the rotation speed and schedule of the TET, which are pre-planned.

To control the GT power output, a PID controller using a feedback signal is usually adopted. The control deviation (i.e., error) is the difference between the process variable and set-point and is used as the feedback signal. As shown in Figure 1 [21], a higher fuel flow rate is required to increase the power output at a given ramp-rate. The turbine inlet temperature (TIT) also increases as the fuel flow rate increases. Due to the time delay of the feedback signal, undershoot and overshoot of the GT's main operation parameters naturally occur. Accordingly, when the power output increases more rapidly, the fuel flow rate and TIT increase more steeply, and the undershoot and overshoot of the main parameters become larger. Factors that limit the ramp-rate include the increase in the maximum TIT, instantaneous increase in rate of change of the TIT, and larger fluctuation in rotation speed.

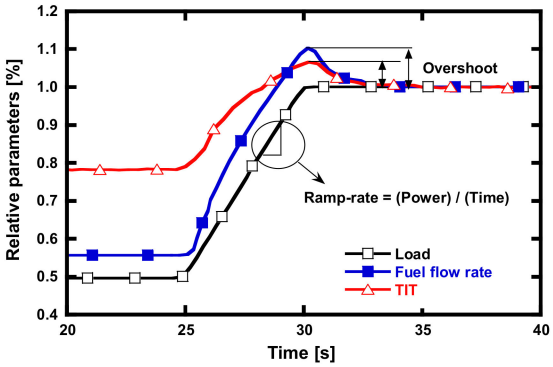

Figure 1. Variations in fuel flow rate and turbine inlet temperature according to load change [21].

A high ramp-rate rapidly changes the main parameters of the GT. Various studies have been conducted to analyze the problems that this causes. A high ramp-rate increases the fluctuation in rotation speed, which increases the frequency fluctuations. It is well-known that the quality of electricity decreases as the frequency fluctuation increases [22]. Studies have been conducted to analyze the change in rotation speed according to the load change [21,23].

A high ramp-rate also increases the turbine temperature rapidly. Studies were conducted to analyze the effect of rapid temperature rise on the hot section of GT components [24]. The effect of the temperature rise of the blades on the creep life was analyzed, and various methods to predict the creep life were studied [25,26]. A study was conducted to suggest a method for calculating the lifetime of components through thermal stress change [27,28]. Changes in thermal stress during start-up and shut-down of a GT were analyzed [29,30]. Kim et al. [31] tried to inject compressed air to prevent the rapid rise of TIT while increasing the ramp-rate. Moon et al. [32] tried to improve the operational flexibility through new control logic based on an artificial neural network (ANN).

1.3. Research Objective

The objective of this study was to reduce the fluctuations of the main operating parameters while increasing the ramp-rate. An advanced control method has been proposed to optimize a set-point schedule for the TET and rotation speed. The schedule is used for the PID control of a conventional GT to increase the ramp-rate. Unlike conventional control, in which the set-point is linear or constant, the advanced control optimally changes the set-point to compensate for the expected overshoot and undershoot.

Through this method, the main operating parameters such as the temperature of the hot part and rotation speed can be stably maintained, even when the power output fluctuates. For quantitative adjustment, the new set-point schedule was optimized using a genetic algorithm. The dynamic behavior was analyzed in a wide range of partial load operation using the advanced control. When the advanced control was applied to the GT in partial load operation, the effect on the dynamic behavior of the main operating parameters was compared with conventional control.

2. GT Simulation Model

2.1. Design Modeling

The target gas turbine in this study was the GE MS7001F-PG7241 (FA) [33]. Figure 2 shows the configuration of the GT model. The GT is composed of inlet and outlet ducts, a compressor, a combustor, and a turbine. A rotating shaft connects the compressor and the turbine. The air flow rate into the compressor inlet is manipulated by changing the angle of the VIGV at the compressor inlet. In a real GT, the compressor and turbine are composed of multiple stages, and some of the compressor inter-stage air is extracted as a turbine coolant. However, information on the flow rate of cooling air and the exact extraction location from the manufacturers is not well-known. Therefore, a simplified model consisting of

a compressor and turbine as a single stage was used in this study. In the model, all the cooling air is extracted from the outlet of the compressor and enters the turbine nozzle and rotor. This modeling method has been used in various studies to predict GT performance, and its rationality and accuracy have been verified [34–36].

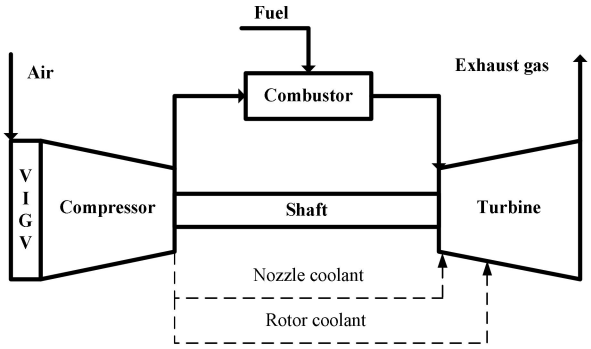

Figure 2. Configuration of the gas turbine.

Table 1 compares the field data and simulation results. Some design parameters that were not measured in operation were referenced from the values of another paper on the same GT [37]. A program developed in MATLAB® [38] was used for the GT simulation. Table 1 shows that the design performance of the simulated GT using the program was almost consistent with the design performance of the operation data. In previous studies, the GT simulation program was verified [37,39]. To accomplish the purpose of this study, some options were added to the program such as improving the correction factor according to the angle of VIGV and optimizing the set-point schedule.

Table 1. Design specifications of the gas turbine.

Parameters	Field Data	In House Code
Ambient temperature [°C]	15	15
Ambient pressure [kPa]	101.325	101.325
Ambient relative humidity [%]	60	60
Air mass flow rate [kg/s]	N/A	421.371 [37]
Compressor pressure ratio [-]	15.2	15.2
Compressor polytropic efficiency [%]	91.84	91.84
Fuel flow rate [kg/s]	9.1437	9.1437
Turbine inlet temperature [°C]	N/A	1397 [37]
Turbine rotor blade inlet temperature [°C]	N/A	1327 [37]
Turbine exhaust gas temperature [°C]	608.1	608.1
Turbine polytropic efficiency [%]	N/A	88.57
Total cooling air flow rate [kg/s]	N/A	81.84
Shaft speed [rpm]	3600	3600
Mechanical efficiency [%]	N/A	99 [37]
Generator efficiency [%]	N/A	98.5 [37]
Net power [MW]	166.4	166.4
Gas turbine Efficiency (LHV) [%]	36.91	36.91

In the program, the conservation of mass and energy conservation equations were used as the governing equations for analysis of all components. All working fluids such as air, fuel, and combustion gas were assumed to be ideal gas mixtures. Enthalpy and entropy were calculated with the polynomial equations of the specific heats of constant pressure provided by NASA [40]. The fuel was natural gas composed of 91.33% methane, 5.36% ethane, 2.14% propane, 0.95% n-butane, and 0.22% nitrogen by volume. The LHV of the fuel is 49,299.1 kJ/kg.

The outlet enthalpy of the combustor was calculated using the energy conservation equation:

$$h_{comb,out} = \frac{(\dot{m}h)_{comb,in} + \eta_{comb}\{\dot{m}(h + LHV)\}_{fuel}}{\dot{m}_{comb,in} + \dot{m}_{fuel}} \quad (1)$$

In Equation (1), the combustor efficiency was determined by assuming heat loss. The method proposed by Kim et al. was used to estimate the cooling air flow rate [37]. The cooling air flow rate was calculated through energy balance of the compressor outlet, combustor, turbine nozzle, and turbine rotor inlet. As a result, the total cooling air flow rate was calculated to be approximately 19.42% of the compressor inlet air flow rate.

The pressure loss of the ducts was set to 0.5% by referring to the literature on the same F-class GT [37]. The output and efficiency of the compressor and turbine were calculated using Equations (2) and (3) under the assumption of steady state. In Equation (2), f is the fraction of rotor cooling air chargeable to turbine power output and was set to 0.5 [32]. The enthalpy of the rotor inlet refers to the enthalpy after the fluids of the turbine inlet, nozzle coolant, and half of the rotor coolant are mixed. The enthalpy of the rotor outlet refers to the enthalpy before mixing of the fluid of the rotor coolant, which does not participate in turbine power output. The power output and efficiency of the GT were calculated using Equation (4).

$$\dot{W}_{comp} = \dot{m}(h_{out} - h_{in}),\ \dot{W}_{turb} = (\dot{m}_{turb,in} + \dot{m}_{NC,in} + f \cdot \dot{m}_{RC,in})(h_{R,in} - h_{R,out}) \quad (2)$$

$$\eta_{comp} = \frac{h_{out,s} - h_{in}}{h_{out} - h_{in}},\ \eta_{turb} = \frac{h_{R,in} - h_{R,out}}{h_{R,in} - h_{R,out,s}} \quad (3)$$

$$\dot{W}_{GT} = \dot{W}_{turb} - \dot{W}_{comp} - \dot{E}_{loss},\ \eta_{GT} = \frac{\dot{W}_{GT}}{\dot{m}_{fuel} \cdot LHV_{fuel}} \quad (4)$$

$\dot{E}_{loss}$ represents all the losses including the generator, mechanical, and heat losses. The heat losses might play a major role in the low-load regime in this study because the data used were for the start-up operation. During the start-up process, a considerable amount of the heat energy is accumulated in the metal due to the large temperature difference [41].

In our analysis, the energy loss of Equation (4) was obtained from the difference in the measured GT power and the simulated GT power using the turbine and compressor modeling. The simulation tried to match the TET and fuel flow rate to the measured values as much as possible. It was confirmed that the energy loss became larger as the GT power decreased. Then, the energy loss was curve-fitted with the GT power and incorporated in the main simulation for various GT operations.

2.2. Off-Design Modeling and Validation

2.2.1. Overview

For all components, the control volume affects the time it takes for the fluid to reach equilibrium. The control volume is very small compared to the velocity of the fluid, so the time to reach equilibrium is very small. Therefore, the overall process of GT analysis can be assumed to be in quasi-equilibrium [32,37,42,43]. The program was verified through off-design performance modeling and prediction under the quasi-equilibrium assumption before the dynamic characteristic analysis of the GT.

2.2.2. Compressor

In the off-design analysis of the compressor, the air flow rate, compressor pressure ratio (CPR), and compressor efficiency are calculated by matching the operating point with the turbine. Working-point matching was conducted using a performance map [44] consisting of the semi-dimensionless mass flow rate, pressure ratio, isentropic efficiency, and rotation speed, as shown in Figure 3. The definitions of each parameter are shown in

Equation (5).

$$M = \frac{\dot{m}\sqrt{T_{in}}}{p_{in}},\ \mathrm{PR}_{comp} = \frac{p_{out}}{p_{in}},\ \Omega = \frac{\sqrt{T_{in}}}{\omega} \tag{5}$$

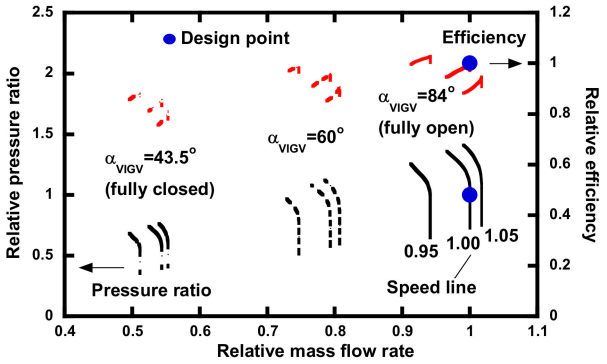

Figure 3. Performance map of the compressor.

The changes of the inlet air flow rate, CPR, and compressor efficiency were performed through scaling of the speed lines according to the change of the IGV angle (α_{VIGV}) in the compressor performance map. The method was basically similar to that used in commercial software such as GateCycle 6.1.2 [45]. Scaling of the speed lines was performed using the correction factors (C_m, C_p, and C_e).

$$M_{corrected} = M_{original} \cdot C_m \tag{6}$$

$$PR_{corrected} = PR_{original} \cdot C_p \tag{7}$$

$$\eta_{corrected} = \eta_{original} \cdot C_e \tag{8}$$

The factors were tuned based on the corresponding GT operation data. Figure 4 shows the variations in the correction factors with α_{VIGV}. C_m and C_p were set to be the same because it has been shown that the changes in air mass flow rate and CPR are nearly equal [36,46].

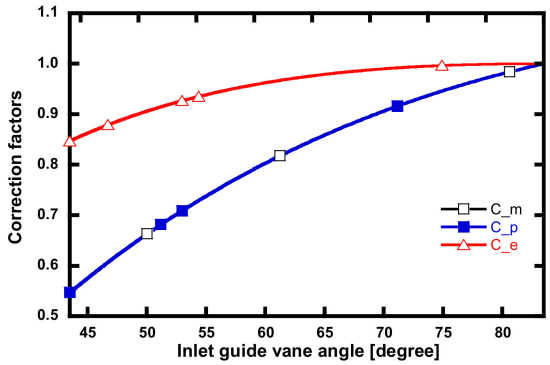

Figure 4. Correction factors of performance map.

2.2.3. Duct

When the operating point changes, the pressure loss also changes. Therefore, Equation (9) was used to correct the change in pressure loss according to the change of inlet flow rate, pressure, and temperature [47].

$$\frac{(\Delta P/P_{in})}{(\Delta P/P_{in})_d} = \frac{\left(\dot{m}\sqrt{T_{in}}/P_{in}\right)^2}{\left(\dot{m}\sqrt{T_{in}}/P_{in}\right)_d^2} \tag{9}$$

2.2.4. Combustor

The combustion was assumed to be complete combustion [48]. Thermal energy loss was reflected via the combustor efficiency. As for the duct, Equation (9) was used to correct the pressure loss according to changes in flow rate, pressure, and temperature.

2.2.5. Turbine

Off-design analysis was conducted using a tuned performance map based on operation data, as shown in Figure 5. The definitions of each parameter are shown in Equation (10).

$$M = \frac{\dot{m}\sqrt{T_{in}}}{p_{in}}, \ \mathrm{PR}_{turb} = \frac{p_{in}}{p_{out}}, \ \Omega = \frac{\sqrt{T}}{\omega} \tag{10}$$

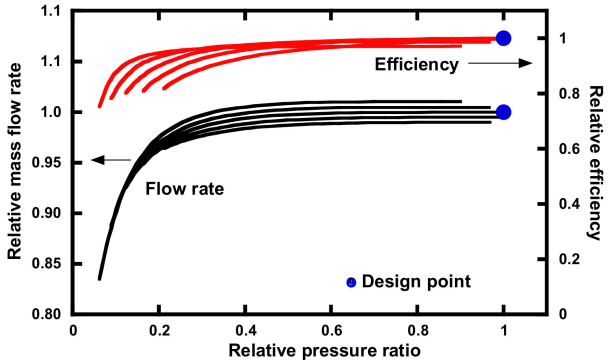

Figure 5. Performance map of the turbine.

The expansion ratio and efficiency were calculated by matching the compressor and operating point. Equation (11) was used to correct the cooling air flow rate according to the change in operating point using [49].

$$\dot{m}_{coolant} = \dot{m}_{coolant,d}\left(\frac{p_{coolant}}{p_{coolant,d}}\right)\left(\frac{T_{coolant,d}}{T_{coolant}}\right)^{0.5} \tag{11}$$

2.2.6. Validation

Figure 6 shows the validation of the model through a comparison of the simulation of the off-design performance and field data. The compared operating variables include the TET, compressor discharge temperature (CDT), CPR, fuel flow rate, compressor air flow rate, and VIGV angle. All of them are expressed as a relative value to the full load value. The right vertical axis shows the absolute value of the VIGV angle.

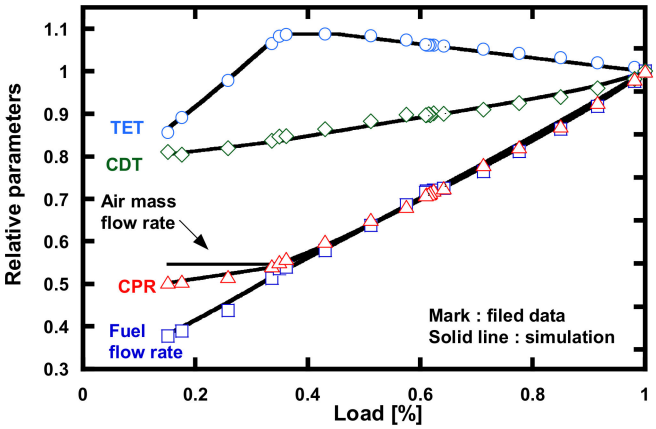

Figure 6. Validation of the simulation of GT operation.

The average error of the off-design simulation under the quasi-equilibrium assumption and operation data is defined in the following equation. The result was within 0.78%, and the off-design performance prediction of the program was verified.

$$Avarage\ \ error(\%) = \frac{\sum_{t=0}^{n} \frac{\left|x_{field}(t) - x_{simulation}(t)\right|}{x_{field}(t)}}{n} \cdot 100 \quad (12)$$

2.3. Dynamic Modeling

2.3.1. Start-Up Data

Figure 7 shows the operation data from when the load of the target GT increases from 15% to 100% during the start-up process. When the load increased from 15% to 35%, the power output was increased with a ramp-rate of 15 MW/min by increasing only the fuel flow rate in the state where the VIGV angle was maximally closed (43.5 degrees). When the load was 35%, the power output was maintained for a while because TET reached 650 °C, which was set as the limit. The power output then increased at a ramp-rate of 12 MW/min until the load reached 60%. There are two important ramp-rates in the start-up sequence: 12 and 15 MW/min. These were used as reference ramp-rates in our analysis and denoted as such in Section 3.

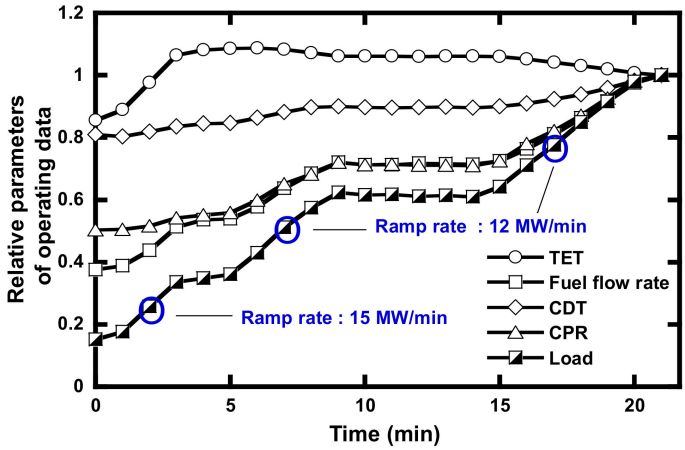

Figure 7. Operating data of the start-up process of the target GT.

At this time, the VIGV angle opens, and the air flow rate into the compressor inlet increases. Thus, the TET is controlled so that it does not exceed 650 °C. When the load reaches 60%, which is the minimum load, the combustor operation mode is changed from diffusion mode to the premix mode [50], and the power output is maintained without increasing for a certain period of time in consideration of the flame stability. At 100% load, the VIGV angle reaches its maximum (84 degrees), which means that the air flow rate also reaches its maximum.

2.3.2. Rotating Inertia

The rotor's time constant is determined by the rotor's moment of inertia and is significantly larger than the volume time constant. Therefore, only the rotating inertia was considered [51]. During load-following operation, the rotation speed of the shaft changes due to imbalance between the load (i.e., power demand) of the generator and the actual power output of the GT. The change in rotation speed was calculated using Equation (13), which reflects the rotating inertia. The rotating inertia was set to 42,000 kgm^2 by referring to the value in the literature on the same F-class GT [37].

$$I\frac{d\omega}{dt} = \left(\dot{W}_{GT} - Load\right) / \left(N \cdot \frac{2\pi}{60}\right) \quad (13)$$

2.3.3. Conventional PID Controller Design (Control Unit)

The control unit of a GT consists of a governor (or controller), an actuator, and a measurement system [52]. In this study, it was assumed that the effect of the delay time of the actuator and measurement system was insignificant, and the governor was assumed to use only a PID controller by referring to various literature on the control system [37,53]. The controller manipulates a manipulated variable to obtain a pre-planned value of a process variable according to the change of the load [19,54]. The process variables are the rotation speed and the TET, and the manipulated variables are the fuel flow rate and the VIGV angle.

The rotation speed of the shaft was controlled to a constant value to generate a constant power frequency of 50 or 60 Hz. The target GT was connected to a power grid with a frequency of 60 Hz. The rotation speed was set to 3600 rpm by controlling the fuel flow through the PID controller. Another PID controller manipulated the VIGV angle to match the TET to a pre-planned control curve. In the control curve, the TET was planned according to the compressor discharge pressure to control the TIT, which is difficult to measure [31,55].

Figure 8 shows measured TET data. Two trends were clearly observed: the TET decreased with increasing compressor discharge pressure (i.e., CPR), but was limited to 650 °C. Based on these observations, the control curve for our simulation was set as the line in the figure.

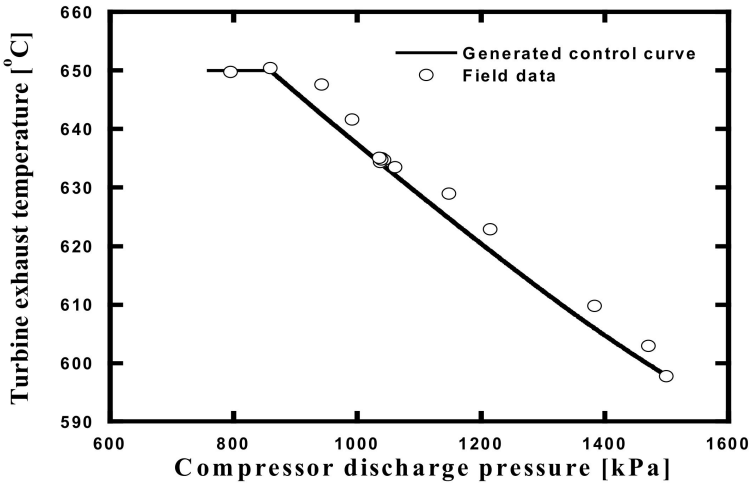

Figure 8. Control curve of the turbine exhaust temperature.

Figure 9 shows the control logic that was applied to the model to simulate partial load operation. When the load changes, the rotation speed changes due to the imbalance of the shaft power and the load of the generator, and the fuel flow rate was manipulated to maintain the rotation speed at the set-point value of 3600 rpm. If the measured TET according to the change in the manipulated fuel flow rate is different from the TET set-point value of the control curve, the VIGV angle is adjusted to match it.

The difference between the process variable and the set-point is called the control deviation or error, and the PID controller uses Equation (14) to obtain the manipulated variable through the control deviation. The proportional gain (KP), integral gain (KI), and derivative gain (KD) values were obtained through trial and error. Based on operation data, only the fuel controller was operated from 15% to 35% of the full load, and the VIGV controller was added at loads of 35% to full load.

$$MV(t+dt) = MV(t) + K_P e(t) + K_I \int_0^\tau e(\tau)d\tau + K_D \frac{de(t)}{dt},\ e(t) = SP - PV \quad (14)$$

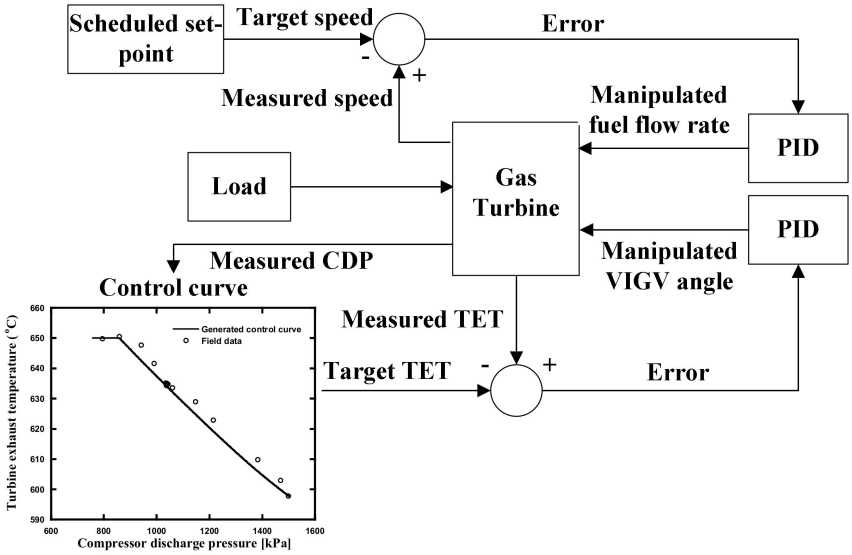

Figure 9. Block diagram of the PID control.

2.3.4. Optimization of the Set-Point Schedule for the Advanced Control

The advanced control proposed in this study used the same control logic as the conventional control but uses an optimized set-point schedule. In the conventional control, the set-point values of the rotation speed and the TET are 3600 rpm and the values from the control curve (the line of Figure 8), respectively. The rotation speed undershoots and the TET overshoots in the conventional control [21,37] when the load to the GT increases. Therefore, when overshoot is expected, the set-point value should be decreased, and when undershoot is expected, the set-point value should be increased so that the values of the process variables (rotation speed and TET) can better follow the target values, which are the set-point values of the conventional control.

Figure 10 illustrates the idea of improving the set-point schedule during the start-up of the target GT. The load profile was exactly the same as that in Figure 7. According to the load profile, the entire start-up sequence can be divided into six sections: A, B, C, D, E, and F. A load-changing section is followed by a constant-load section. The pattern repeats three times (A/B, C/D, and E/F) and reaches the full load condition.

Figure 10a illustrates the set-point schedule of the rotation speed. The dotted line with unfilled square marks is the original rotation speed set-point of the conventional control. The solid line with solid square marks is an arbitrary (or interim) set-point schedule in the middle of the optimization process, which is shown here only for the purpose of illustrating the idea of the advanced control. The set-point schedule consists of set-point values.

For optimization of the set-point schedule of the rotation speed, the set-point schedule was changed to reduce the overshoot and undershoot. The optimization of the schedule was performed by a genetic algorithm, which will be explained later in this section. It is clear from the figure that the set-point value changes, converges to a certain value, and returns to the set-point value of conventional control (see processes A/B, C/D, and E/F).

The targets for optimization were three parameters of the load-changing periods (A, C, and E): the maximum change of the set-point value, the shape of the change, and the duration of the change. Similarly, in sections B, D, and F, the parameters for optimization were selected as the shape of the change of the return of the set-point value to that of the conventional control and the duration of the change.

Figure 10b illustrates the set-point schedule of the TET. The dotted line with unfilled square marks is the original set-point of the conventional control, while the line with solid square marks is an example (or arbitrarily interim setting) of the new set-point schedule. The TET schedule was studied only for sections C through F because the VIGV control was not used in sections A and B. In sections C and E, the initial value and the decreasing slope

of the set-point were selected as the parameters for optimization. In sections D and F, the original set-point values were used as they were because the load was constant, so there was no overshoot or undershoot.

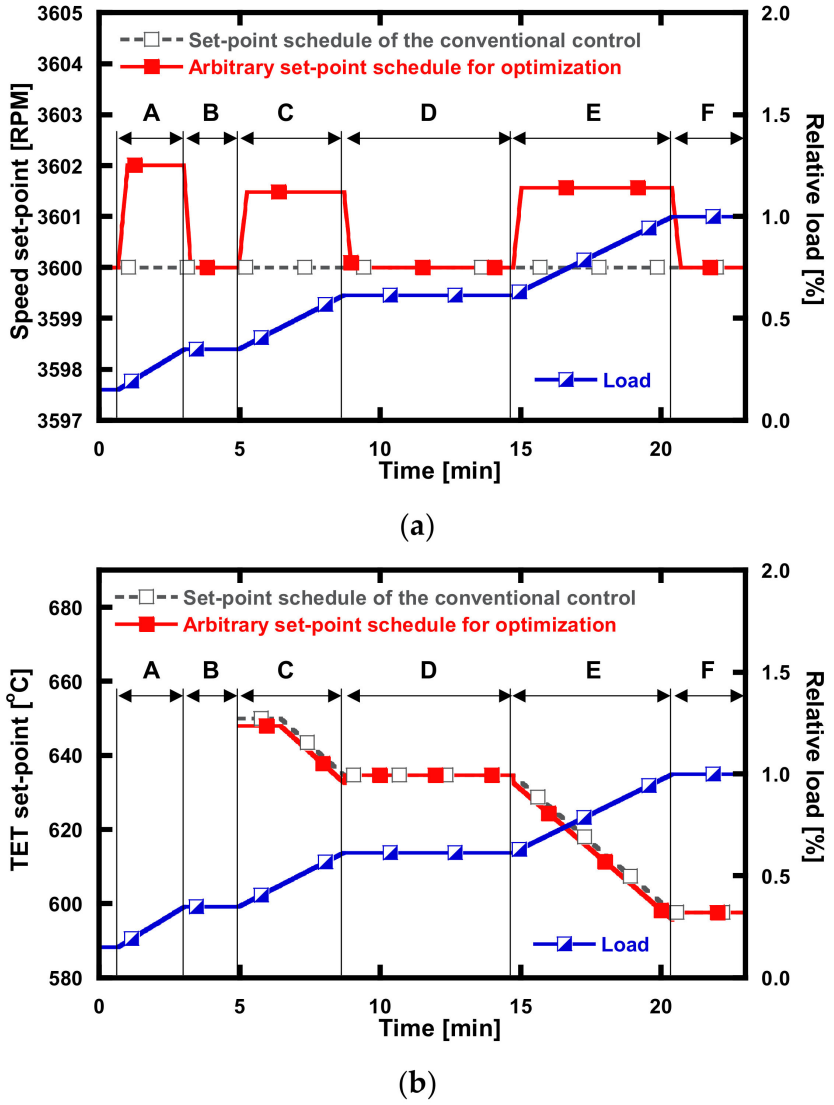

Figure 10. Examples of rotation speed and TET set-point schedules. (**a**) Rotation speed. (**b**) TET.

The objective function for the optimization is defined in Equations (15) and (16). The objective function is the sum of the deviation, which is the difference between the set-point value of the conventional control and the value of the process variable simulated with the change in set-point value. When the deviation is a negative value, it means that undershoot occurs, and when it is a positive value, it means that overshoot occurs. A value of deviation close to zero indicates that the undershoot and overshoot are minimized.

$$deviation_{new,i}(t) = PV_{new,i}(SP_{new,i}(a, b, c, \cdots, t)) - SP_{conventional,i}(t) \tag{15}$$

where, i = 1: corresponding to speed, i = 2: corresponding to TET, a: maximum change, b: shape of change, c: duration of change, t: time

$$obj = \sqrt{\frac{1}{n}\sum_{i=1}^{2}\sum_{t=1}^{n}(deviation_{new,i}(t))^2} \tag{16}$$

The set-point schedule was optimized using the optimization toolbox provided by MATLAB® [38]. A genetic algorithm was used to solve the optimization problem of a multivariate function. The genetic algorithm searches for solutions using Darwin's theory of evolution and the principles of natural selection and survival of the fittest. Conventional optimization techniques have many local optimal points, whereas a genetic algorithm can overcome this disadvantage by probabilistically searching for a solution. Since genes are designated as individual parameters, it is easy to solve an optimization problem of multivariate functions.

The optimization process of the genetic algorithm is shown in Figure 11, where small squares represent genes. A combination of genes is called a chromosome, and a group of chromosomes is defined as a population. An initial generation with a random population is formed, and the fitness of each chromosome of the initial generation is evaluated. In the fitness assessment, a suitable chromosome is selected, and the population of the next generation is determined through processes called crossover and mutation. This evolutionary process goes through several generations to obtain the optimal chromosome [56].

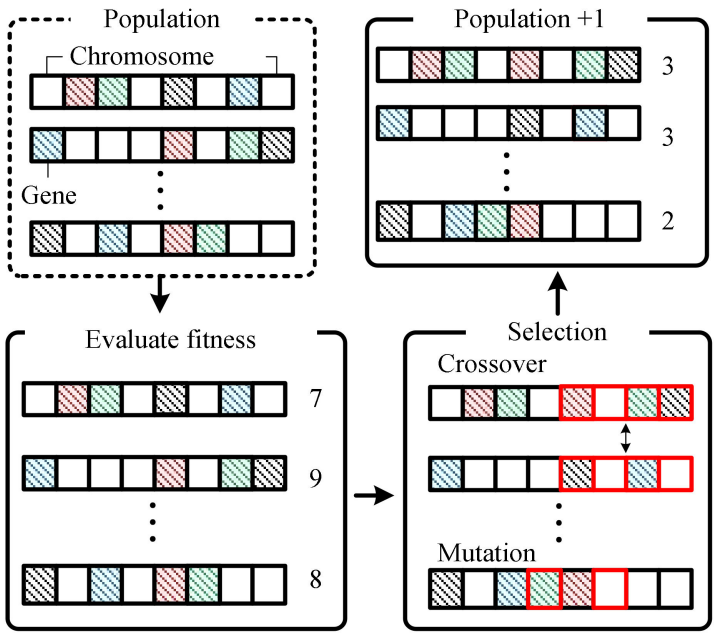

Figure 11. Flow chart of the genetic algorithm.

Figure 12 shows the concept of the optimization process of the set-point schedule through the genetic algorithm and illustrates an arbitrary generation. Figure 12a,b show the optimizing processes of the speed set-point schedule in section A and the TET set-point schedule in sections C and E, respectively. Sections D and F in Figure 12b are expressed as a single point because the TET does not change in these sections.

The value of the objective function in Equation (16) is minimized as the set-point schedule changes. In the figure, a gene is a set-point value at a certain time in the set-point schedule. Chromosomes A, B, C, D, E, and F are sets of genes and are each an arbitrary set-point schedule. For each chromosome, the optimal genes are selected through the evolution process, and the objective function value is gradually minimized in the next generation. As a result, the optimal solution is selected as the set-point schedule with the minimum value of the objective function in the last generation.

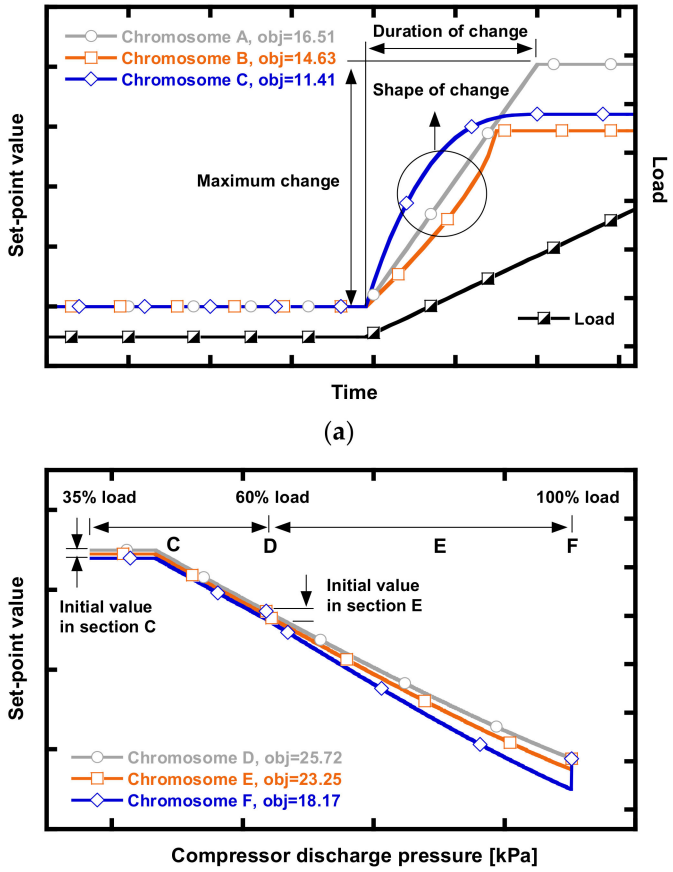

Figure 12. Set-point schedules in an arbitrary generation. (**a**) Rotation speed. (**b**) TET.

3. Results and Discussion

3.1. Impact of the Optimized Control

Figure 13 shows the impact of the optimized control using the simulated results of a part of the start-up sequence in Figure 10. Figure 13a shows the details of the optimized speed set-point schedule in sections A and B of Figure 10a. The optimized set-point schedule of the rotation speed had a trapezoidal shape. It was confirmed that the maximum change in the schedule increased as much as the maximum undershoot of the speed obtained with the conventional control.

The optimized set-point value gradually increased in the form of an arc until the set-point value converged to the maximum change. The duration of change in section A was 21 s. When the load started to become constant, the optimized set-point value gradually decreased in the form of an arc. The duration of change in section B was 15 s.

Figure 13b shows the details of the optimized TET set-point schedule on the control curve in sections C and E. It was confirmed that the optimized set-point value decreased as much as the overshoot in the conventional control. In addition, the set-point value follows the set-point value of the conventional control again when the load becomes constant.

3.2. Effect of Using the Advanced Control for the Reference Ramp-Rates

Figures 14 and 15 show the dynamic behavior simulated by the advanced control for the entire start-up process and the comparison with those obtained by the conventional control. Figure 14 shows the results of the optimized set-point schedules of the rotation speed and TET as well as the predicted deviations of the two process variables. In Figure 14a, the maximum changes of the optimized speed set-point in sections C and E (the second and third changes) were different from that in section A (the first change; see Figure 13 for the details of section A). This occurs because the maximum undershoot of the conventional

control varies according to the ramp-rate. The durations of change were 19, 14, 18, and 17 s in sections C, D, E, and F, respectively. In Figure 14b, the TET set-point had to be decreased more significantly as the full load approached. This occurs because the air flow rate changes rapidly, and the overshoot of the TET increases in the conventional control as the full load approaches.

Figure 15 compares the variations in the main operating parameters between the conventional and advanced controls. The fuel flow rate and VIGV angle are expressed as relative values to those at full load. First, the results of the conventional control are discussed. When the load first increases at 15%, which corresponds to the beginning of section A, the load becomes higher than the power output momentarily due to the delay time of the controller. The rotation speed is temporarily reduced. More fuel flow rate is required due to the decrease in the rotation speed. The power output increases to be almost equal to the load as the fuel flow increases. If there is no VIGV angle change, the TET and TIT also increase due to the increase in the fuel flow rate. The load then becomes constant at 35% (section B), the rotation speed recovers quickly from the undershoot, and it returns to the equilibrium state.

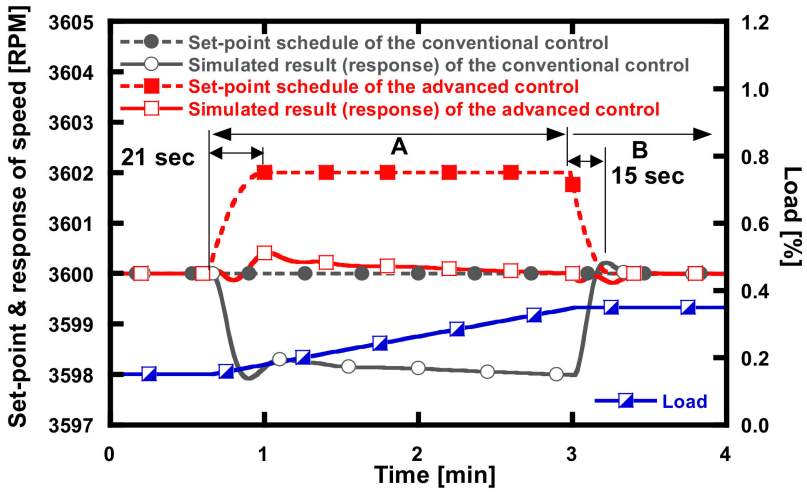

(a)

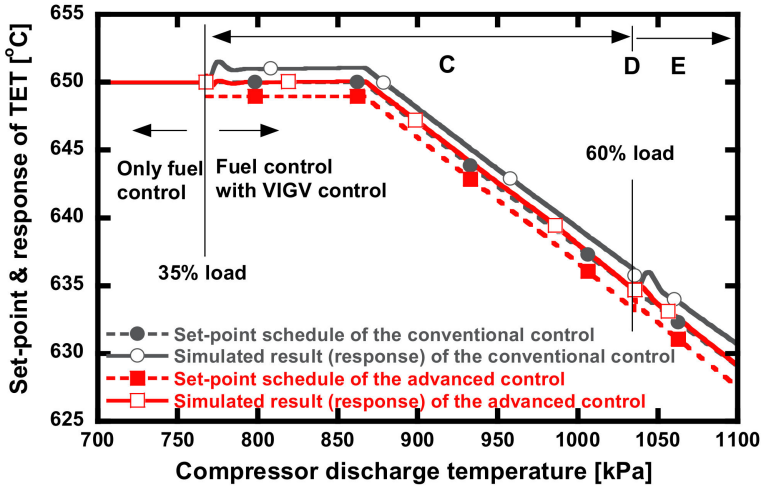

(b)

Figure 13. Impact of the optimized set-point schedules. (**a**) Rotation speed. (**b**) TET.

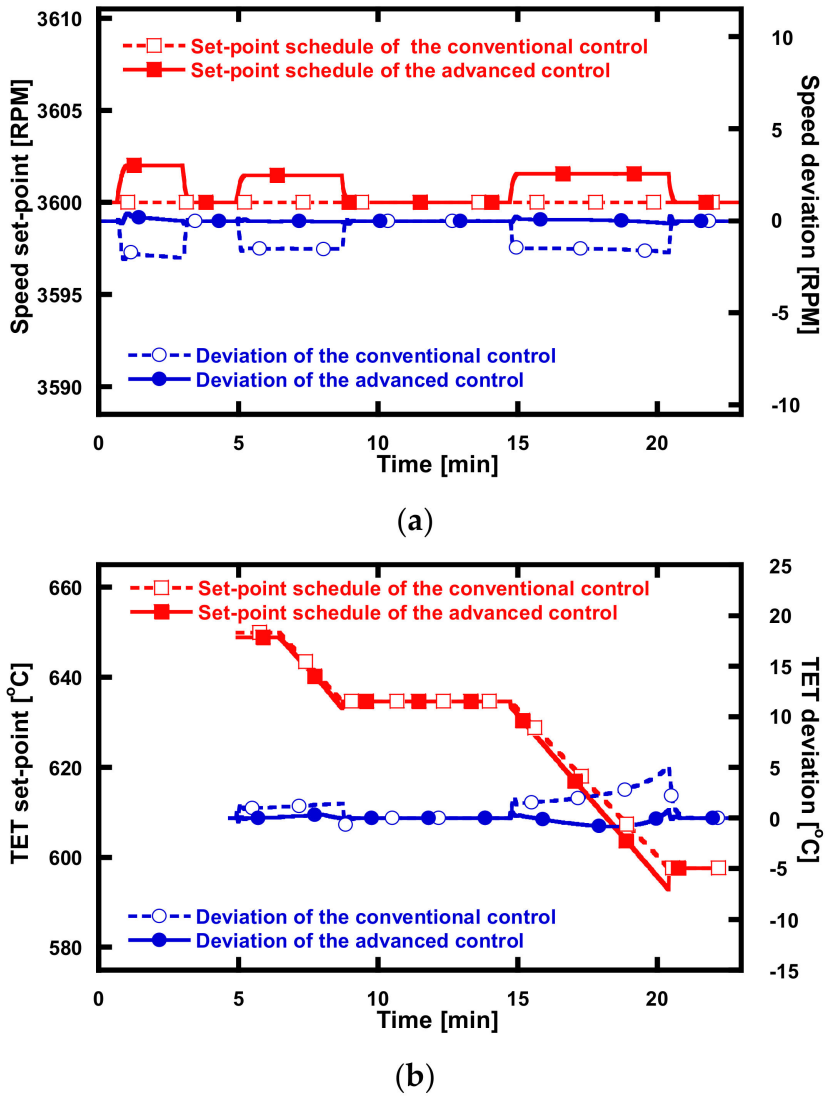

Figure 14. Set-point schedules and deviations of rotation speed and TET for the entire start-up process with reference ramp rates (15 MW/min and 12 MW/min). (**a**) Rotation speed. (**b**) TET.

The power output momentarily becomes higher than the load due to the delay time of the controller, and overshoot of the fuel flow rate, TIT, and TET occurs, as shown in the dotted line of the enlarged part of Figure 15a. When the load increases above 35% (section C), the VIGV angle is adjusted to control the TET according to the planned schedule. The VIGV angle opens, and the TIT slowly increases compared to the section where the load is less than 35% because the air flow rate increases. When the load becomes constant at 60% (section D), the TET and TIT recover quickly from overshoot and return to the equilibrium state. When the full load is reached, the overshoot of the TIT is the maximum value because the change in air flow rate is large and rapid, as shown in the dotted line of the enlarged part of Figure 15b (sections E and F).

Next, the results of the advanced control are explained. The general trend is the same as that of the conventional control, but a striking difference was observed in the maximum deviations. In the enlarged parts of the figure, the maximum deviations of both the rotation speed and the TET decreased. The undershoot of the rotation speed and the overshoot of the TET were much smaller than with the conventional control. For this reason, the optimized set-point schedule makes the manipulated variable change more quickly in Equation (14). The fuel flow rate begins to increase more quickly, and the VIGV angle opens more quickly as the load begins to increase, while the fuel flow converges to the

equilibrium value quickly. Furthermore, the VIGV angle closes more quickly once the load increase stops (see the solid line of the enlarged part of Figure 15b).

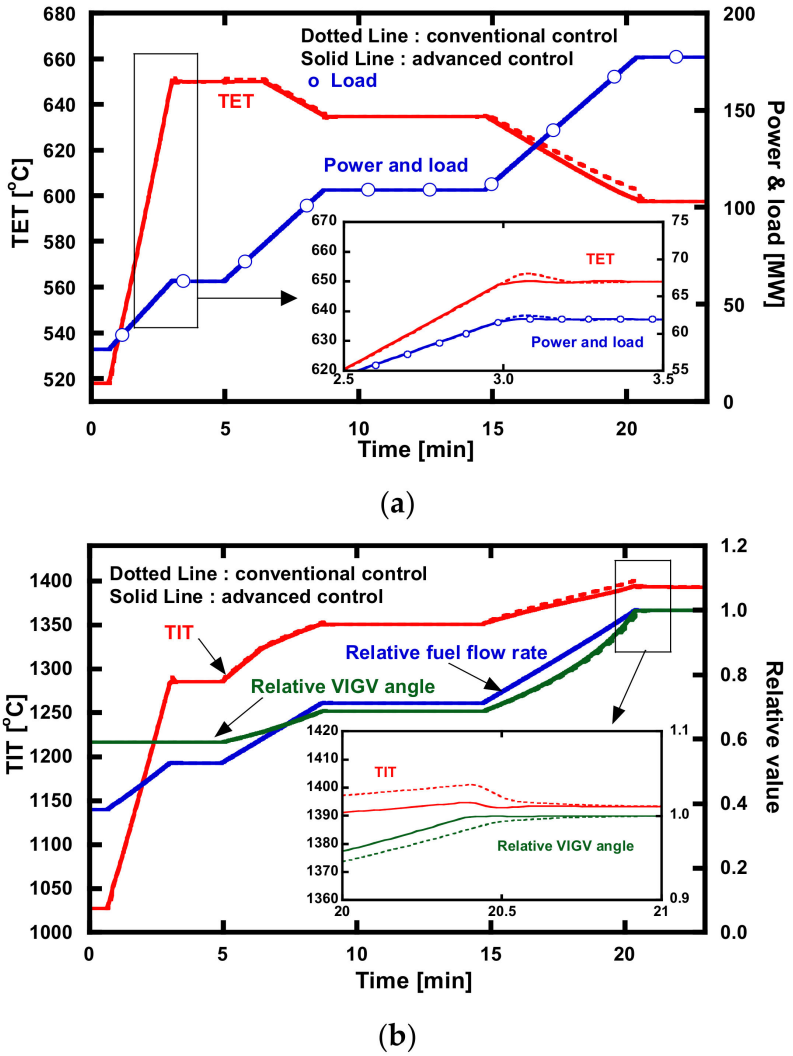

Figure 15. Variations in the operating parameters for the entire start-up process with reference ramp rates (15 MW/min and 12 MW/min). (**a**) Load, power, and TET. (**b**) Relative VIGV angle, relative fuel flow rate, and TIT.

When comparing the advanced control with the conventional control, the maximum difference between the power demand (load) and actual power output decreased from 0.54 MW (0.30%) to 0.23 MW (0.13%). The maximum speed deviation decreased from 2.08 rpm (0.06%) to 0.41 rpm (0.01%). The ratios are relative to the full load values. The maximum TET decreased by 2.3 °C from 652.8 °C to 650.5 °C, and the maximum TIT decreased by 6.3 °C from 1401.1 °C to 1394.8 °C. The maximum rate of change of the TIT at full load was decreased from 0.7 °C/s to 0.4 °C/s. The reduction in all these fluctuations, especially those of the TIT, would play an important role in preventing blade damage while improving the ramp-rate.

3.3. Effect of Using the Advanced Control for an Increased Ramp-Rate

The advantage of the advanced control is expected to be greater as the required ramp-rate becomes larger. Accordingly, a case was simulated with a ramp-rate of 50 MW/min, which is much higher than the reference rates, and results are presented in Figures 16 and 17. Figure 16 shows the results of the optimized set-point schedules and predicted deviations

of the rotation speed and TET, and Figure 16 compares the variations in the main operating parameters between the conventional and advanced controls.

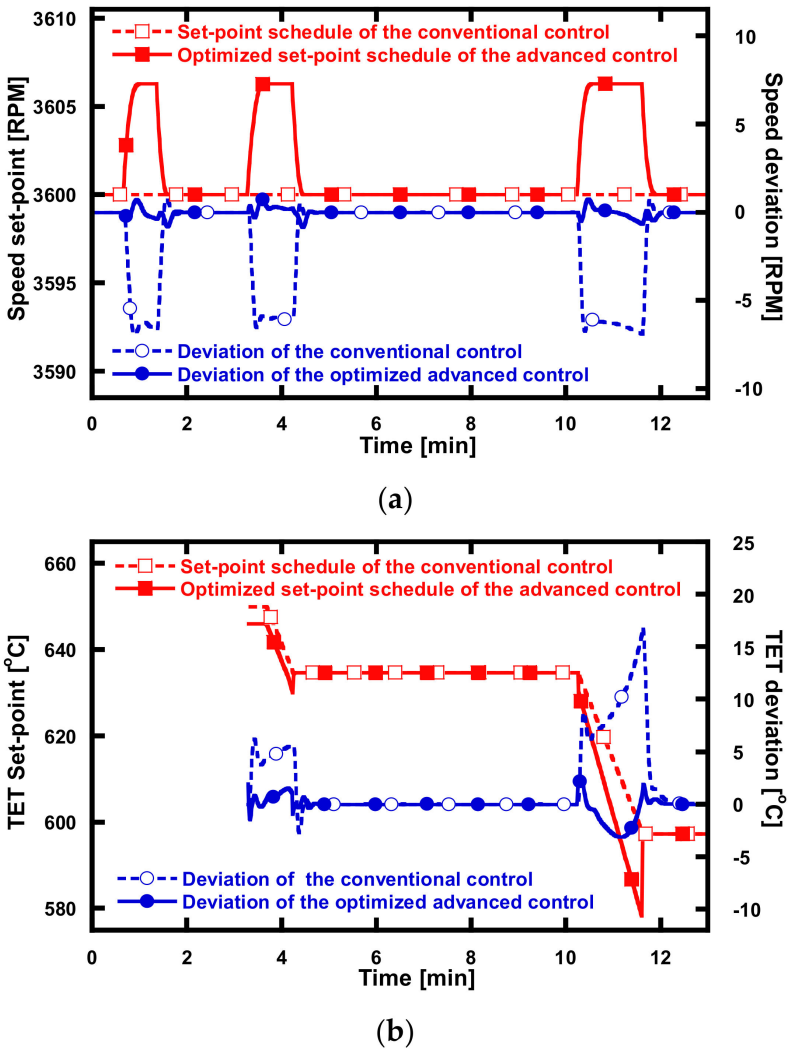

Figure 16. Set-point schedules and deviations of rotation speed and TET for the entire start-up process with an increased ramp rate (50 MW/min). (**a**) Rotation speed. (**b**) TET.

The trends are similar to those in Figures 14 and 15 for the reference ramp-rates, and all the operating parameters changed more rapidly. Thus, the change in the set-point values of the rotation speed and TET should also be larger. With the conventional control, there was a larger difference between the power demand (load) and power output at the end of the load increasing period (see the enlarged parts of the figure) in comparison to the case of the reference ramp-rate (Figures 15a and 17a). Therefore, the overshoot and undershoot also becomes larger. Consequently, the maximum TIT of the conventional control was as high as 1418.6 °C, which is 17.5 °C higher than that of the reference case (1401.1 °C). The maximum speed deviation increased from 2.08 rpm (0.06%) in the reference case to 6.92 rpm (0.20%). These results clearly show the negative side of increasing the ramp-rate and show why the ramp-rate should be limited.

From Figures 16 and 17, it is clear that the advanced control would be very effective in decreasing all the deviation, especially those related to temperatures. The maximum difference between the power demand (load) and actual power output was decreased from 2.19 MW (1.24%) to 0.76 MW (0.42%) by adopting the advanced control. The maximum speed deviation decreased from 6.93 rpm (0.19%) to 0.84 rpm (0.02%). The maximum TET decreased by 7.3 °C from 659.2 °C to 651.9 °C. The maximum TIT decreased more

significantly by 22.7 °C from 1418.6 °C to 1395.9 °C. The maximum rate of change of the TIT at full load also showed a large decrease from 2.3 °C/s to 0.6 °C/s.

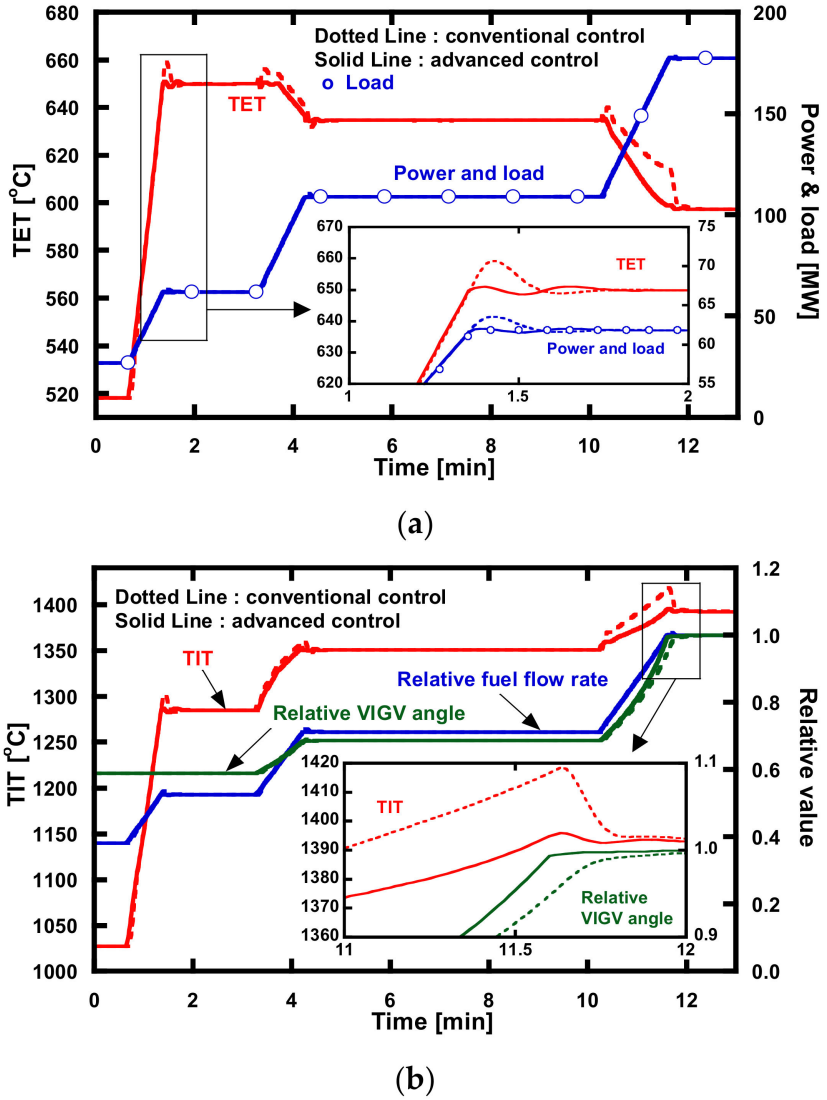

Figure 17. Variations in the operating parameters for the entire start-up process with an increased ramp rate (50 MW/min). (**a**) Load, power, and TET. (**b**) Relative VIGV angle, relative fuel flow rate, and TIT.

Table 2 summarizes the quantitative results of the major factors for various operation strategies. The advantage of the advanced control becomes clearer when we compared the results of the advanced control for a ramp-rate of 50 MW/min to those of the conventional control for the reference ramp-rates (12 and 15 MW/min). Even though the ramp-rate was increased by more than three times, with the advanced control, all of the major factors were much lower. The maximum speed deviations were 2.08 rpm (0.06%) and 0.84 rpm (0.02%), the maximum TITs were 1401.1 °C and 1395.9 °C (more than 5 °C reduction), and the maximum rates of TIT change at full load were 0.7 °C/s and 0.6 °C/s. These results verify that the advanced control enables a significantly higher ramp-rate while reducing the fluctuations of all the operating parameters or at least maintaining them at their original levels.

Table 2. Results of the major factors for the operation strategies.

Parameters (Maximum Value)	Reference Ramp-Rates (15 MW/min and 12 MW/min)		Increased Ramp-Rate (50 MW/min)	
	Conventional Control	Advanced Control	Conventional Control	Advanced Control
$\dot{W}_{GT} - Load$ [%]	0.30	0.13	1.24	0.42
Speed deviation [%]	0.06	0.01	0.19	0.02
TET [°C]	652.8	650.5	659.2	651.9
TIT [°C]	1401.1	1394.8	1418.6	1395.9
Rate of TIT change [°C/s]	0.7	0.4	2.3	0.6

4. Conclusions

In this study, an advanced control was proposed to suppress the overshoot of the TIT to improve the ramp-rate of a GT. The advanced control used optimized set-point schedules that minimized fluctuations in the rotation speed and TET. The optimized set-point schedules were derived using a genetic algorithm.

The key to the optimized set-point schedule is to decrease the set-point value in a section where overshoot occurs in the conventional control and to increase the set-point value in a section where undershoot occurs. Thus, the advanced control suppresses the occurrence of overshoot and undershoot of the operating parameters. Furthermore, it is possible to reduce the rate of change of the TIT at full load.

When the load increased, the advanced control significantly reduced the fluctuations in the rotation speed and TET compared to the conventional control. This occurred because the manipulated variables (such as the fuel flow rate and VIGV angle) changed more rapidly through the set-point adjustment. In addition, even when the ramp-rate was increased by more than three times the reference values to 50 MW/min, the advanced control decreased the maximum fluctuation of the rotation speed by 40% and decreased the maximum TIT by 5.2 °C compared with the operation using the conventional control at the reference ramp-rate. Furthermore, the rate of change of the TIT was reduced from 0.7 °C/s to 0.6 °C/s at full load.

These results confirm that the advantage of the advanced control becomes clearer as the ramp-rate becomes larger. It would enable a significantly higher ramp-rate while even reducing the fluctuations of all the operating parameters. There are three major expected advantages of using the advanced control: (1) improving the quality of electricity; (2) extending the lifespan of high-temperature components; and (3) the possibility of improving the ramp-rate. First, it is possible to reduce the fluctuation of the rotation speed caused by the change in the power output of the GT. This has the effect of improving the quality of the electricity produced by the GT because it reduces the frequency fluctuations. Second, the reduction in the TIT fluctuation reduces the thermal stress applied to the high-temperature components, so the lifespan of the high-temperature components can be extended. Third, even if the ramp-rate is increased by more than three times, the fluctuations of the rotation speed and TIT are reduced in comparison to when using the conventional control at the reference ramp-rate.

In conclusion, a strong possibility of stably improving the ramp-rate using the advanced control was found. As a result, the advanced control is expected to be effectively utilized when more flexible operation of a GT is required with the expansion of renewable energy. Possible future studies include (1) simulation of the control of the GT in the lower load and start-up regimes and (2) technology to shorten the start-up time by stably controlling the temperature.

Author Contributions: Conceptualization, Y.-K.P., S.-W.M., and T.-S.K., Methodology, Y.-K.P. and S.-W.M., Software, Y.-K.P. and S.-W.M., Formal analysis, Y.-K.P., Investigation, Y.-K.P. and S.-W.M., resources, T.-S.K., data curation, Y.-K.P., writing—original draft, Y.-K.P., Writing—review and editing, Y.-K.P., S.-W.M., and T.-S.K., Supervision, T.-S.K., Project administration, T.-S.K.; Funding acquisition, T.-S.K. All authors have read and agreed to the published version of the manuscript.

Funding: This work was supported by the Korea Institute of Energy Technology Evaluation and Planning (KETEP) and the Ministry of Trade, Industry and Energy (MOTIE) of the Republic of Korea (No.20193310100050).

Institutional Review Board Statement: Not applicable.

Informed Consent Statement: Not applicable.

Conflicts of Interest: The authors declare no conflict of interest.

Nomenclature

C	*Correction factor*
$\dot{E}$	Energy
e	Error
f	Fraction of rotor coolant chargeable to power
h	Specific enthalpy (kJ/kg)
I	Rotating inertia (kg·m^2)
K	Gain
Load	Load (kW)
M	Semi-dimensionless mass flow rate (kg·K$^{0.5}$/kN·s)
$\dot{m}$	Mass flow rate (kg/s)
MV	Manipulated variable
N	Rotation speed (rpm)
obj	Objective function
P	Pressure (kPa)
PR	Pressure ratio
PV	Process variable
SP	Set-point
s	Specific entropy (kJ/kg)
T	Temperature (°C)
t	Time (sec)
$\dot{W}$	Power (kW)
Greek	
α	Inlet guide vane angle (°)
η	Efficiency (-)
Ω	Semi-dimensionless speed (rpm/K$^{0.5}$)
ω	Rotation speed (rad/s)
Subscripts	
Coolant	Cooling air flow
Comb	Combustor
Comp	Compressor
Conventional	Conventional value
Corrected	Corrected value
D	Derivative
d	Design
e	Efficiency
field	Field data
fuel	Fuel flow
GT	Gas turbine
I	Integral
in	Inlet
loss	Losses
m	mass flow rate
N	Nozzle
NC	Nozzle coolant
new	New value
original	Original value

out	Outlet
P	Proportional
p	Pressure ratio
R	Rotor
RC	Rotor coolant
ref	Reference
shaft	Shaft
s	Isentropic
simulation	Simulation data
turb	Turbine

Abbreviations

ANN	Artificial neural network
CDT	Compressor discharge temperature (°C)
CPR	Compressor pressure ratio
GT	Gas turbine
LHV	Lower heating value (kJ/kg)
PID	Proportional-integral-derivative
P2G	Power to gas
P2L	Power to liquid
RMSD	Root mean square deviation
TET	Turbine exhaust temperature (°C)
TIT	Turbine inlet temperature (°C)
VIGV	Variable inlet guide vane

References

1. International Energy Agency. *World Energy Outlook*; International Energy Agency: Paris, France, 2020; pp. 1–464.
2. Wang, Y.; Silva, V.; Lopez-Botet-zulueta, M. Impact of high penetration of variable renewable generation on frequency dynamics in the continental Europe interconnected system. *IET Renew. Power Gener.* **2016**, *10*, 10–16. [CrossRef]
3. Sinsel, S.R.; Riemke, R.L.; Hoffmann, V.H. Challenges and solution technologies for the integration of variable renewable energy sources—A review. *Renew. Energy* **2020**, *145*, 2271–2285. [CrossRef]
4. Isaiah, T.G.; Dabbashi, S.; Bosak, D.; Sampath, S.; Di Lorenzo, G.; Pilidis, P. Life Analysis of Industrial Gas Turbines Used as a Back-Up to Renewable Energy Sources. *Procedia CIRP* **2015**, *38*, 239–244. [CrossRef]
5. Jenkins, J.D.; Zhou, Z.; Ponciroli, R.; Vilim, R.B.; Ganda, F.; de Sisternes, F.; Botterud, A. The benefits of nuclear flexibility in power system operations with renewable energy. *Appl. Energy* **2018**, *222*, 872–884. [CrossRef]
6. Wang, B.; Zhang, C.; Dong, Z.Y.; Li, X. Improving Hosting Capacity of Unbalanced Distribution Networks via Robust Allocation of Battery Energy Storage Systems. *IEEE Trans. Power Syst.* **2021**, *36*, 2174–2185. [CrossRef]
7. Bizon, N.; Hoarcă, I.C. Hydrogen saving through optimized control of both fueling flows of the Fuel Cell Hybrid Power System under a variable load demand and an unknown renewable power profile. *Energy Convers. Manag.* **2019**, *184*, 1–14. [CrossRef]
8. Ulbig, A.; Borsche, T.S.; Andersson, G. Impact of low rotational inertia on power system stability and operation. *IFAC Proc.* **2014**, *19*, 7290–7297. [CrossRef]
9. Johnson, S.C.; Papageorgiou, D.J.; Mallapragada, D.S.; Deetjen, T.A.; Rhodes, J.D.; Webber, M.E. Evaluating rotational inertia as a component of grid reliability with high penetrations of variable renewable energy. *Energy* **2019**, *180*, 258–271. [CrossRef]
10. Ulbig, A.; Rinke, T.; Chatzivasileiadis, S.; Andersson, G. Predictive control for real-time frequency regulation and rotational inertia provision in power systems. In Proceedings of the IEEE Conference on Decision and Control, Firenze, Italy, 10–13 December 2013; pp. 2946–2953. [CrossRef]
11. Boubenia, A.; Hafaifa, A.; Kouzou, A.; Mohammedi, K.; Becherif, M. Carbone dioxide capture and utilization in gas turbine plants via the integration of power to gas. *Petroleum* **2017**, *3*, 127–137. [CrossRef]
12. Albrecht, F.G.; Konig, D.H.; Dietrich, R.U. The potential of using power-to-liquid plants for power storage purposes. In Proceedings of the International Conference on the European Energy Market, EEM, Porto, Portugal, 6–9 June 2016; pp. 1–5. [CrossRef]
13. Ahn, J.H.; Jeong, J.H.; Kim, T.S. Performance Enhancement of a Molten Carbonate Fuel Cell/Micro Gas Turbine Hybrid System with Carbon Capture by Off-Gas Recirculation. *J. Eng. Gas Turbines Power* **2019**, *141*, 1–10. [CrossRef]
14. Bexten, T.; Wirsum, M.; Rosche, B.; Schelenz, R.; Jacobs, G. Model-Based Analysis of a Combined Heat and Power System Featuring a Hydrogen-Fired Gas Turbine with On-Site Hydrogen Production and Storage. In Proceedings of the ASME Turbo Expo, virtual, 21–25 September 2020.
15. California Independent System Operator. *What the Duck Curve Tells Us about Managing a Green Grid*; California Independent System Operator: Folsom, CA, USA, 2016.

16. Scottmadden Inc. *Revisiting the California Duck Curve*; ScottMadden: Atlanta, GA, USA, 2016.
17. GE GAS POWER. OpFlex* Advanced Control Solutions. 2021. Available online: https://www.ge.com/content/dam/gepower-new/global/en_US/downloads/gas-new-site/products/digital-and-controls/opflex/opflex-brochure.pdf (accessed on 25 November 2021).
18. Power Engineering International. Siemens Blends Past and Present for Next Generation Gas-Fired Power Efficiency. 12 January 2018. Available online: https://www.powerengineeringint.com/coal-fired/siemens-blends-past-and-present-for-next-generation-gas-fired-power-efficiency/ (accessed on 20 November 2021).
19. Rowen, W.I. Simplified mathematical representations of single shaft gas turbines in mechanical drive service. In Proceedings of the ASME International Gas Turbine and Aeroengine Congress and Exposition, Cologne, Germany, 1–4 June 1992.
20. Kim, T.S. Comparative analysis on the part load performance of combined cycle plants considering design performance and power control strategy. *Energy* **2004**, *29*, 71–85. [CrossRef]
21. Camporeale, S.M.; Fortunato, B.; Mastrovito, M. A modular code for real time dynamic simulation of gas turbines in simulink. *J. Eng. Gas Turbines Power* **2006**, *128*, 506–517. [CrossRef]
22. Baggini, A. *Handbook of Power Quality*; Wiley: New York, NY, USA, 2008; ISBN 9780470754238.
23. Kavalerov, B.V.; Bakhirev, I.V.; Kilin, G.A. An investigation of adaptive control of the rotation speed of gas turbine power plants. *Russ. Electr. Eng.* **2016**, *87*, 607–611. [CrossRef]
24. Townsend, R.; Winstone, M.; Henderson, M.; Nicholls, J.R.; Partridge, A.; Nath, B.; Wood, M.; Viswanathan, R. *Life Assessment of Hot Section Gas Turbine Components*; Cambridge University Press: Cambridge, UK, 2000; pp. 37–38. Available online: https://www.scopus.com/record/display.uri?eid=2-s2.0-85064348601&origin=inward (accessed on 20 November 2021).
25. Mohamed, W.; Eshati, S.; Pilidis, P.; Ogaji, S.; Laskaridis, P.; Nasir, A. A method to evaluate the impact of power demand on HPT blade creep life. In Proceedings of the ASME Turbo Expo, Vancouver, QC, Canada, 6–10 June 2011; Volume 4, pp. 1–45092.
26. Abdul Ghafir, M.F. Performance Based Creep Life Estimation for Gas Turbine Application. Ph.D. Thesis, Cranfield University, Bedford, UK, 2011. Available online: https://ethos.bl.uk/OrderDetails.do?uin=uk.bl.ethos.566015 (accessed on 20 November 2021).
27. Benato, A.; Bracco, S.; Stoppato, A.; Mirandola, A. LTE: A procedure to predict power plants dynamic behaviour and components lifetime reduction during transient operation. *Appl. Energy* **2016**, *162*, 880–891. [CrossRef]
28. Wood, M.I. Gas turbine hot section components: The challenge of 'residual life' assessment. *Proc. Inst. Mech. Eng. Part A J. Power Energy* **2000**, *214*, 193–201. [CrossRef]
29. Rossi, I.; Source, A.; Traverso, A. Gas turbine combined cycle start-up and stress evaluation a simplified dynamic approach. *Appl. Energy* **2017**, *190*, 880–890. [CrossRef]
30. Poursaeidi, E.; Bazvandi, H. Effects of emergency and fired shut down on transient thermal fatigue life of a gas turbine casing. *Appl. Therm. Eng.* **2016**, *100*, 453–461. [CrossRef]
31. Kim, M.J.; Kim, T.S. Feasibility study on the influence of steam injection in the compressed air energy storage system. *Energy* **2017**, *141*, 239–249. [CrossRef]
32. Moon, S.W.; Kim, T.S. Advanced Gas Turbine Control Logic Using Black Box Models for Enhancing Operational Flexibility and Stability. *Energies* **2020**, *13*, 5703. [CrossRef]
33. Eldrid, R.; Kaufman, L.; Marks, P. *The 7FB: The Next Evolution of the F Gas Turbine*; GE Power Systems: Schenectady, NY, USA, 2001.
34. Gay, R.R.; Palmer, C.A.; Erbes, M.R. *Power Plant Performance Monitoring*; Techniz Books International: New Delhi, India, 2006; pp. 110–116. ISBN 0-9755876-0-9.
35. Moon, S.W.; Kwon, H.M.; Kim, T.S.; Kang, D.W.; Sohn, J.L. A novel coolant cooling method for enhancing the performance of the gas turbine combined cycle. *Energy* **2018**, *160*, 625–634. [CrossRef]
36. Lee, J.H.; Kim, T.S. Novel performance diagnostic logic for industrial gas turbines in consideration of over-firing. *J. Mech. Sci. Technol.* **2018**, *32*, 5947–5959. [CrossRef]
37. Kim, J.H.; Kim, T.S.; Moon, S.J. Development of a program for transient behavior simulation of heavy-duty gas turbines. *J. Mech. Sci. Technol.* **2016**, *30*, 5817–5828. [CrossRef]
38. MathWorks Inc. *MATLAB R2021a*; MathWorks Inc.: Natick, MA, USA, 2021; Available online: https://mathworks.com/products/matlab.html (accessed on 20 November 2021).
39. Kim, M.J.; Kim, J.H.; Kim, T.S. Program development and simulation of dynamic operation of micro gas turbines. *Appl. Therm. Eng.* **2016**, *108*, 122–130. [CrossRef]
40. McBride, B.J.; Zehe, M.J.; Gordon, S. *NASA Glenn Coefficient for Calculating Thermodynamic Properties of Individual Species*; Glenn Research Center: Cleveland, OH, USA, 2002.
41. Petkovic, D.; Banjac, M.; Milic, S.; Petrovic, M.V.; Wiedermann, A. Modelling the transient behaviour of gas turbines. In Proceedings of the ASME Turbo Expo, Phoenix, AZ, USA, 17–21 June 2019; pp. 1–91008.
42. Agrawal, R.K.; Yunis, M. A generalized mathematical model to estimate gas turbine starting characteristics. In Proceedings of the ASME Turbo Expo, Houston, Texas, USA, 9–12 March 1981; pp. 194–202.
43. Saravanamuttoo, H.I.; MacIsaac, B.D. The use of a hybrid computer in the optimization of gas turbine control parameters. *Asme J. Eng. Power* **1973**, *95*, 257–264. [CrossRef]
44. GasTurb GmbH. *GasTurb12*; GasTurb GmbH: Aachen, Germany, 2012.
45. GE Energy. *GateCycle ver. 6.1.2.*; General Electric: Boston, MA, USA, 2013.

46. Tarabrin, A.P.; Schurovsky, V.A.; Bodrov, A.I.; Stalder, J.P. Influence of axial compressor fouling on gas turbine unit performance based on different schemes and with different initial parameters. *Am. Soc. Mech. Eng.* **1998**, *78651*, 317–325. [CrossRef]
47. Saravanamuttoo, H.I.; Rogers, G.F.C.; Cohen, H. *Gas Turbine Theory*; Pearson Education: London, UK, 2001; ISBN 978-1292093093.
48. Turns, S.R. *An Introduction to Combustion: Concepts and Applications*, 2nd ed.; McGraw-Hill: New York, NY, USA, 2000; ISBN 10:007235044X.
49. Palmer, C.A.; Erbes, M.R. Simulation Methods Used to Analyze the Performance of the GE PG6541B Gas Turbine Utilizing Low Heating Value Fuels. In Proceedings of the ASME Cogen Turbo Power, Portland, OR, USA, 25–27 October 1994; pp. 1–8.
50. Zucca, A.; Khayrulin, S.; Vyazemskaya, N.; Shershnyov, B.; Myers, G. Development of a liquid fuel system for GE MS5002E gas turbine: Rig test validation of the combustor performance. In Proceedings of the ASME Turbo Expo, Düsseldorf, Germany, 16–20 June 2014; pp. 1–8. [CrossRef]
51. Lahyani, A.; Boughaleb, Y.; Qjani, M. Dynamic Model of a Two Shaft Heavy-Duty Gas Turbine with Variable Geometry. In Proceedings of the International Gas Turbine and Aeroengine Congress and Exposition, Houston, TX, USA, 5 June 1995.
52. Kim, J.H.; Song, T.W.; Ro, S.T. Model development and simulation of transient behavior of heavy duty gas turbines. *J. Eng. Gas Turbines Power* **2001**, *123*, 589–594. [CrossRef]
53. Panov, V. Gasturbolib—Simulink library for gas turbine engine modelling. In Proceedings of the ASME Turbo Expo, Orlando, FL, USA, 8–12 June 2009; Volume 1, pp. 555–59389.
54. Bank Tavakoli, M.R.; Vahidi, B.; Gawlik, W. An educational guide to extract the parameters of heavy duty gas turbines model in dynamic studies based on operational data. *IEEE Trans. Power Syst.* **2009**, *24*, 1366–1374. [CrossRef]
55. Rowen, W.I. Operating characteristics of heavy-duty gas turbines in utility service. In Proceedings of the ASME Turbo Expo, Birmingham, UK, 2–5 June 1988; pp. 5–150.
56. MathWorks, Inc. *Global Optimization Toolbox: User's Guide (R2021b)*; MathWorks Inc.: Natick, MA, USA, 2021; Available online: https://www.mathworks.com/help/pdf_doc/gads/gads.pdf (accessed on 20 November 2021).